Electronic Supplementary Material (ESI) for Journal of Materials Chemistry C.

Electronic Supplementary Information

Tracking a photo-switchable surface-localised supramolecular interaction *via* refractive index

Richard M. Parker,[a,b*] Dominic J. Wales,[a,b] James C. Gates,[b] Peter G. R. Smith[b] and Martin C. Grossel[a]

[a] Chemistry Department, University of Southampton, Highfield, Southampton, UK, SO17 1BJ

[b] Optoelectronics Research Centre, University of Southampton, Highfield, Southampton, UK, SO17 1BJ

* E-mail: rmp53@cam.ac.uk

S1: INSTRUMENTATION

Melting points (MP) were measured using an electrothermal melting point apparatus and are uncorrected. Electrospray mass spectra (MS) were recorded using a Micromass Platform II single quadrapole mass spectrometer. Nuclear magnetic resonance spectra (NMR) were collected using either a Bruker AV300 spectrometer, or a Bruker DPX400 spectrometer; operating at 300 or 400 MHz respectively for ^{1}H NMR experiments and at 75 or 100 MHz for ^{13}C and Dept-135 NMR experiments. ^{13}C NMR spectra were collected fully decoupled. Infrared spectra (IR) were collected on a Nicolet 380 FT-IR spectrometer with a SmartOrbit Golden Gate Attenuated Total Reflection (ATR) attachment. UV-visible spectra absorption were collected using a Shimadzu UV-1601 UV-visible spectrophotometer running UVPC version 3.5. Absorption-based photoisomerisation studies were stimulated with a UVP UVGL-25 dual wavelength UV-lamp (4 W, 254/365 nm). Photoisomerisation of the Bragg grating device was achieved using a custom casing, mounted with switchable ultraviolet (λ_{max} = 370 nm, $\Delta\lambda_{1/2}$ = 12 nm) and blue (λ_{max} = 464 nm, $\Delta\lambda_{1/2}$ = 22 nm) LED light sources (P_d = 40 mW).

S2: ABSORPTION SPECTRUM OF 4-PHENYLAZOPHENOXYACETIC ACID, 3

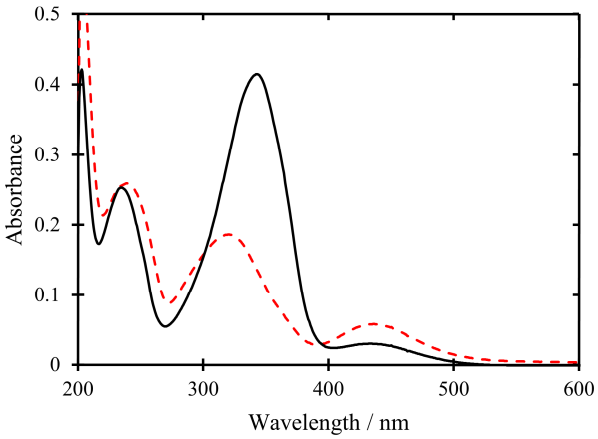

Figure S1. The absorption spectra for the *cis*-isomer (red dashed line) and *trans*-isomer (black line) of 4-phenylazophenoxyacetic acid, **3** (2.5 x 10^{-5} mol dm^{-3} in methanol): *cis* (λ_{max} = 320.5, 450.5 nm) and *trans* (λ_{max} = 342.0 nm).

S3: ^{1}H NMR STUDIES OF α-CYCLODEXTRIN WITH 4-PHENYLAZOPHENOXYACETIC ACID, 3

The relative populations of the photostationary states for **3** (defined here as the point at which further irradiation with UV light at 365 nm does not result in further changes in the absorption spectrum) were investigated by ^{1}H NMR spectroscopy. The chemical shift of the aromatic protons of an azobenzene dye can differ by as much as 1 ppm between the two isomers, with this separation sufficient to distinguish between these isomeric states. Through use of the integrals the *cis*:*trans* ratio can be calculated (Figure S2).

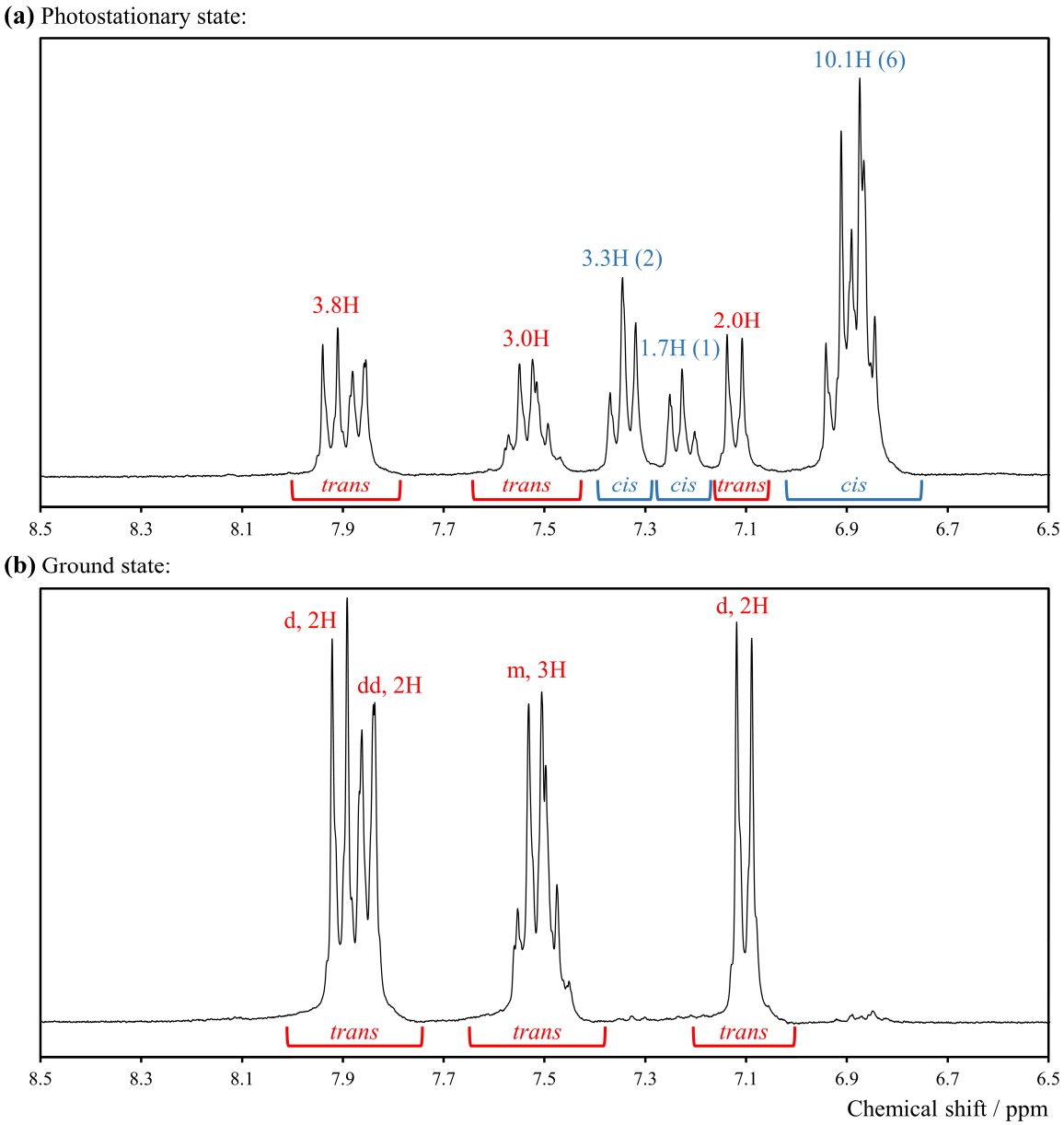

Figure S2. The aromatic regions of the ^{1}H NMR spectrum for 4-phenylazophenoxyacetic acid, **3**, in deuterated methanol: **(a)** at the photostationary state and **(b)** after thermal reconversion back to the initial state (*trans*-isomer). The *cis:trans* ratio is calculated to be 63:37 at the photostationary state.

^{1}H NMR spectra for a mixture of α-cyclodextrin and **3** are shown in Figure S3. Upon addition of **3** to α-cyclodextrin as a 1:1 mixture, broadening of the hydroxyl peaks of the α-cyclodextrin is observed with a corresponding 0.05-0.07 ppm downfield shift of the aromatic azobenzene peaks. Photoisomerisation of the azobenzene to as little as 30% *cis*-isomer by exposure to UV light at 365 nm wavelength is sufficient to re-sharpen these hydroxyl peaks, indicating disruption of the host-guest complex.

Figure S3 (page S-4). The ^{1}H NMR spectra in d_6-DMSO for **(a)** 4-phenylazophenoxyacetic acid, **3**; from the integrals the tr*ans:cis* ratio is 96:4. **(b)** α-cyclodextrin, highlighting the hydroxyl protons. **(c)** Adding **3** to α-cyclodextrin as a 1:1 mixture. **(d)** Photoisomerisation of the azobenzene in this mixture to 30% *cis*-isomer, by exposure to UV light at 365 nm.

(a) 4-phenylazophenoxyacetic acid, **3**

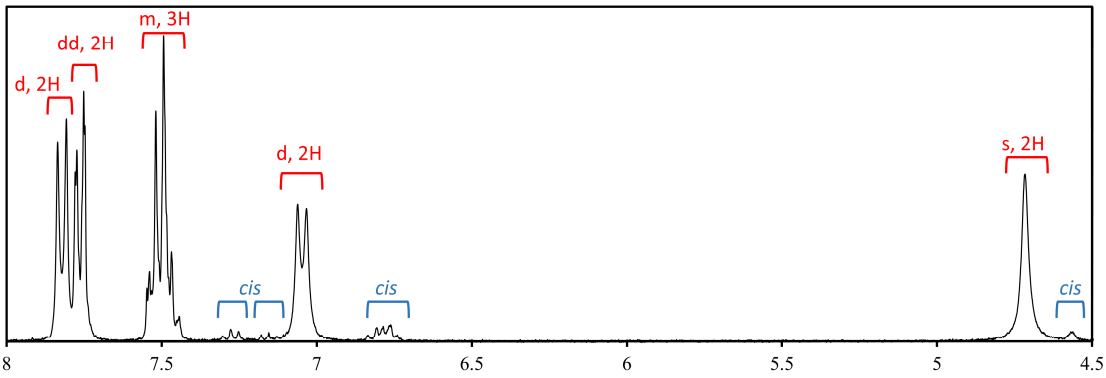

(b) α-cyclodextrin

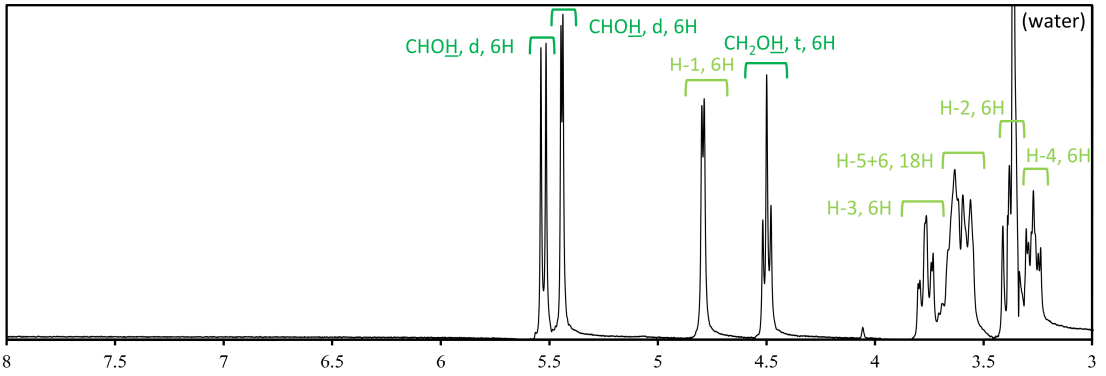

(c) α-cyclodextrin and 4-phenylazophenoxyacetic acid, **3**

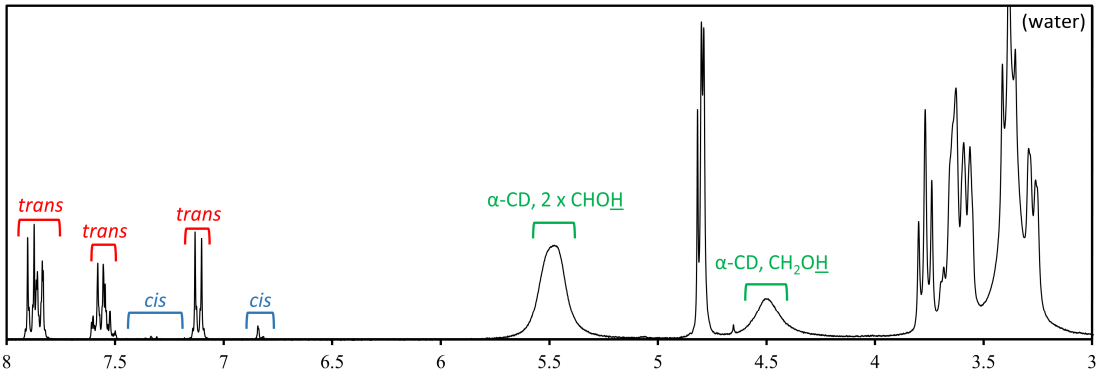

(d) α-cyclodextrin and 4-phenylazophenoxyacetic acid, **3** **- after exposure to UV light (365 nm)**

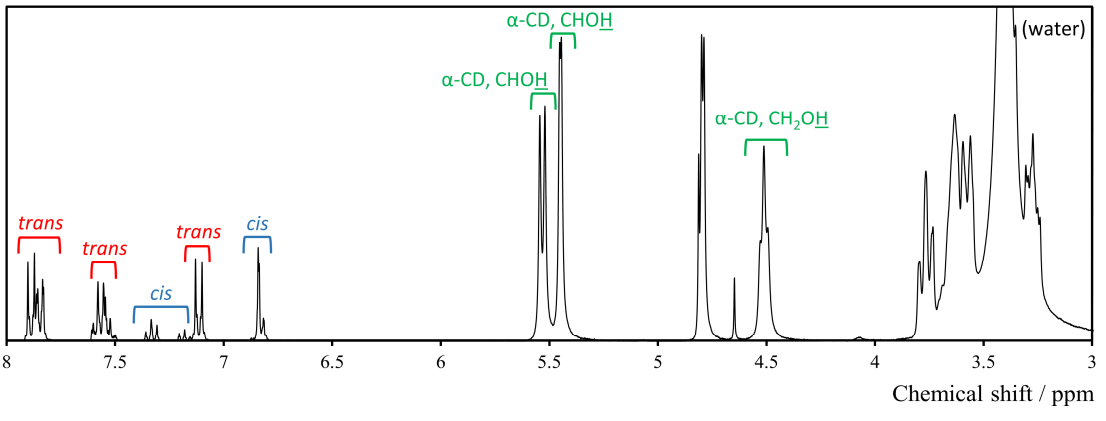

S4: OPTICAL DEVICE FABRICATION

Instrumentation

Direct UV writing of waveguides was performed using a "Cambridge Laser Laboratories" Lexel 95 SHG UV laser combined with an Aerotech ABL9000 air-bearing stage. Tantalum pentoxide was deposited using an OPT plasmalab 400 Sputter system (τ = 10mT, P = 300W, t = 33 min). For interrogation at 1535-1575 nm the waveguide was exposed to an Exfo IQ-2300 erbium fibre-based ASE source as part of an Exfo IQ-203 Optical Test system. The resultant signal was collected by an Ando AQ 6317B optical spectrum analyser (OSA) controlled via a PC running LabVIEW 8.2.1.

Microfluidic pumping was achieved by a Bio-Chem Fluidics solenoid operated micro-pump 130SP1210-1TP, with a 10 µL PTFE chamber, pumping up to 1.2 mL/min. Solutions were switched with a Cole Parmer PTFE manifold mixing solenoid valve, with six inputs leading to one output, capable of transporting 14 L/min at 20 psi. These were connected by Cole Parmer Chemfluor ETFE tubing, with an internal diameter of 0.016" (400 µm) and external diameter of 1/16". Connections were made using Omnifit Omni-Lok Type P fittings, a chemically inert flangeless fitting with a permanently attached PTFE ferrule rated up to 1000 psi.

Fabrication of Integrated Optical Bragg gratings

One route to fabricate a wide range of integrated optical devices is the process of direct UV writing.[1] This technique is based on the local refractive index increase of a photosensitive planar glass layer upon exposure to a tightly focused UV-laser beam. The translation of this beam relative to the substrate allows for the definition of two-dimensional waveguiding structures such as splitters, couplers and Mach-Zehnder interferometers, without the need for photolithographic or subsequent processing. Through a further modification to this technique, Bragg gratings can be simultaneously incorporated directly into the waveguide. Fabrication is achieved by generating a periodic intensity pattern at the focal point of two interfering UV laser beams.[2] By controlling the modulation of this interference pattern, the form of the grating can be precisely controlled. By altering the period of this modulation multiple gratings can be written over a wide wavelength range within a single waveguide channel.[3]

For this work, a three-layer planar glass structure was fabricated on to a silicon substrate by flame hydrolysis deposition (CIP, Ipswich, UK), comprising of under-cladding, core and over-cladding layers with a total silica layer thickness of approx. 40 µm. The 6 µm thick core layer was doped with germanium to raise its refractive index above that of the cladding and to also introduce photosensitivity. The dimensions of this planar device was 10.0 x 20.0 mm.

The waveguiding structure was UV-written into the core layer of this planar glass construction, with its dimensions defined by the thickness of the core layer and the width of the focal point of the interfering UV laser beam (giving rise to a cross-section of approx. 6 x 6 µm). When the device was translated through the UV beams a channel waveguide was written, however, through controlled modulation of this interference pattern Bragg gratings could also be formed selectively along the waveguide. Precise control of this modulation of the laser intensity during fabrication of the periodic grating structure results in an apodised Bragg grating (i.e. the gratings fringe visibility changes with position). In this work the intensity profile of the modulated Bragg grating structure was defined by a Gaussian envelope, giving rise to Gaussian-apodised Bragg peaks in the reflected spectrum (Figure 2, manuscript). Four Bragg gratings were written into a single waveguiding channel, each Bragg grating being 2 mm long and with a period between 529 and 542 nm, satisfying the Bragg condition (Eqn. S1) to reflect at wavelengths between 1535 and 1575 nm.

A commercial optical fibre 'pigtail' was aligned and robustly attached to the integrated Bragg grating device *via* a commercially available 'v-groove' optical fibre assembly and an optical grade UV-cured adhesive, with low insertion loss. This allows for the sensor device to be connected to the optical interrogation system by standard optical fibre connections.

To access the evanescent mode of the waveguide a micro-channel was etched into the overclad with hydrofluoric acid/hydrochloric acid (4:3:9 HF:HCl:H_2O), with real-time feedback (final etch depth: 18 µm). It should be noted that while etching does lead to mismatch of the optical mode between the etched and unetched regions, leading to optical loss, the strength and quality of the Gaussian-apodised Bragg gratings prevents this having any effect on precisely determining the Bragg wavelength.

The surface of the etched well was mechanically polished with an alkali, colloidal silica solution (Logitech Ltd SF1) for 20 – 30 seconds. This was immediately washed with copious amounts of deionised water and dried. Finally, tantalum pentoxide (80 (±4) nm) was sputtered over the etched region.

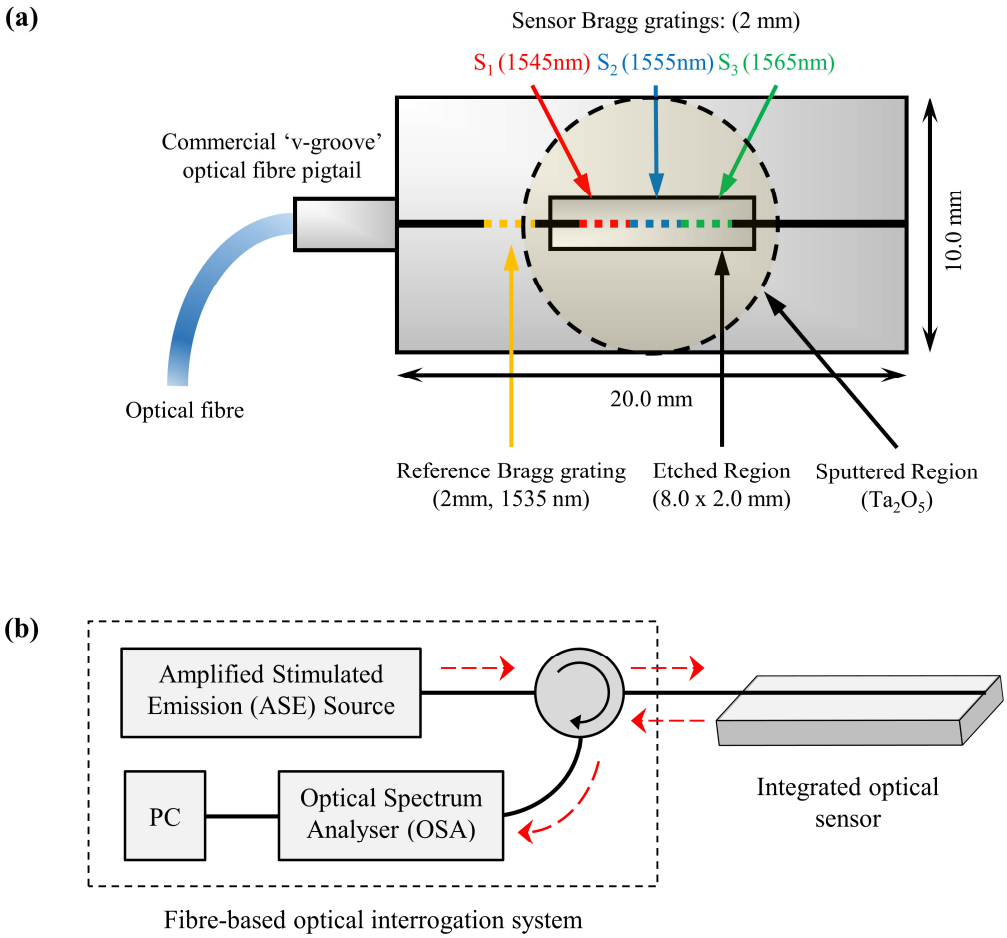

Figure S4. (a) A schematic of an etched and fibre coupled Bragg grating sensor, showing the exposed Bragg grating within the window. **(b)** The readout system is connected to the chip using standard optical fibre and is robustly pigtailed using standard telecom assembly techniques.

Optical Interrogation

A broadband Amplified Spontaneous Emission (ASE) source was used to illuminate the sensor and the circulator allowed the reflected signal to be directed to the optical spectrum analyser (OSA), which was controlled remotely *via* a PC running LabVIEW (Figure S4). Each Bragg grating reflects a characteristic Bragg peak at a wavelength (λ_B) dependent on its local refractive index and grating period, as given by the Bragg condition:

$$\lambda_B = 2n_{eff}.\Lambda \qquad \text{(Eqn. S1)}$$

where n_{eff} is the effective refractive index of the Bragg grating (i.e. the average refractive index experienced by the optical guided mode) and Λ is the period of the refractive index modulation of the grating structure. The spectral shape of the reflected Bragg peak is dictated by any deviation from a uniformly periodic grating structure; in this work this was modulated to result in the reflected peak describing a Gaussian-apodised profile. It should also be noted that the high sensitivity to refractive index reported in this work is made possible through the high spectral fidelity of these Gaussian-apodised Bragg gratings.

By etching the waveguide cladding, the evanescent field of the optical mode within the grating is exposed, allowing changes in the refractive index of the environment to alter n_{eff}. The corresponding shift in the peak Bragg wavelength

can be used to detect these changes in surface-localised refractive index. The Bragg wavelength can be determined from the reflected spectrum, which in this work focuses upon the telecommunication wavelengths (1535-1575 nm). To extract this information, a custom LabVIEW program was written to spectrally identify and fit a Gaussian profile to each reflected Bragg peak. From the equation of the fitted Gaussian the central Bragg wavelength (λ_B) could be determined and its shift with changes in refractive index tracked with time. As this is an absolute measurement of a physical property it does not require continued monitoring and can be compared between experiments, however it should be noted that n_{eff} and λ_B is presented in this work as a shift relative to an initial value, i.e. Δn_{eff}, and $\Delta\lambda_B$, rather than as an absolute refractive index.

The sensitivity of the device to changes in refractive index is strongly dependent on the fraction of the evanescent field that penetrates into the analyte. The etched sensor was calibrated against a series of reference Cargille refractive index liquids (Series AA and AAA), both before and after deposition of a thin-film of tantalum pentoxide (80 nm). As exemplified in Figure 2 in the manuscript, the presence of this thin-film of high-index material dramatically increases the sensitivity of the device, with the sensitivity to bulk refractive index change found to be in the order of 10^{-6}. The peak wavelength of the perpendicular transverse magnetic (TM) and transverse electric (TE) optical modes are different. For the purposes of these experiments the TE mode was selected as this has a higher sensitivity in the presence of a high-index overlayer (Figure 2c), with the much less sensitive TM mode used for *in situ* thermal compensation.[4] It should be noted that while the buried 'reference' grating can be used to accurately track temperature fluctuations during the experiment, a simple first-order deduction of the Bragg wavelength shift is not appropriate in experiments where the thermo-optic constant of the analyte media is non-zero (e.g. when immersed in a liquid).

Microfluidic flow cell:

The microfluidic flow cell was milled from stainless steel and sealed on top of the planar optical device with a Kalrez™ O-ring, this was found to be resilient to common solvents, acids and bases.[5] Fluid flow was controlled by a PTFE diaphragm pump upstream of the flow cell. To select the desired reagent, a PC-controlled six-way PTFE diaphragm valve was incorporated into the system and connected *via* 400 µm bore ETFE tubing (Figure S5).

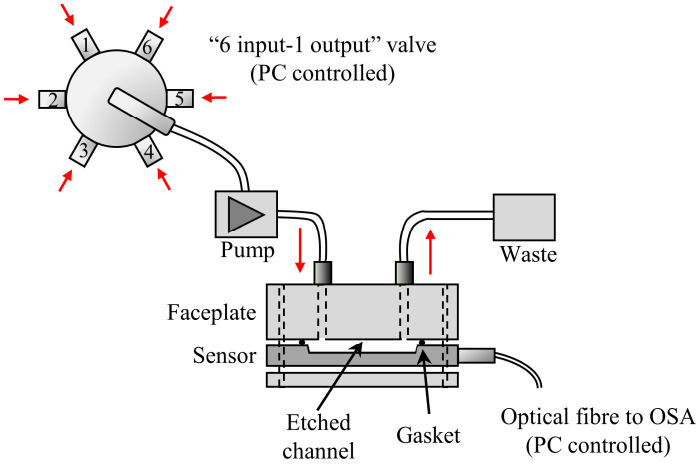

Figure S5. A schematic of the integrated optical Bragg grating sensor device, within the microfluidic flow cell network.

S5: PREPARATION OF A SELF-ASSEMBLED MONOLAYER

Deposition of a self-assembled monolayer of (3-aminopropyl)triethoxysilane

The functionalisation of the sensor surface within the micro-channel consisted of cleaning and preparative steps, followed by chemical reaction and optical calibration against a known reference solution. Within the microfluidic flow cell each of these individual steps can be concatenated into a single, automated recipe that was applied sequentially to the micro-reactor. The period of the pump and the switching of reservoirs was controlled using a custom LabVIEW script connected *via* a USB DAQ controller. Each of the five stock solutions were freshly prepared

and connected to a separate inlet to the microfluidic system and air bubbles cleared from the tubing. By switching the valve, solutions were then selectively drawn through the micro-reactor and over the sensor surface, as given by the following recipe. A constant pump period was used throughout the experiment of 4.0 s, corresponding to a pump rate of 0.15 mL/min. This was a continuous process and was conducted as a single experiment, monitored in real-time *via* the Bragg grating sensor.

The typical recipe used to clean and functionalise the surface was as follows:

1)	deionised water	30 minutes
2)	acetone	30 minutes
3)	deionised water	30 minutes
4)	potassium hydroxide (5.0 M)	60 minutes
5)	deionised water	20 minutes
6)	ethanol (reference)	80 minutes
7)	10 % 3-APTES in ethanol	720 minutes
8)	ethanol (reference)	80 minutes

The two alcohol washes were used as a comparative reference, allowing for the change in the effective refractive index of the waveguide to be calculated upon surface functionalisation with 3-APTES.

Attachment of 4-Phenylazophenoxyacetyl chloride (4) to a 3-APTES monolayer surface

A large excess of **4** (~ 50 mg) was dissolved in dimethylsulfoxide (70 mL), to this was added triethylamine (<0.1 mL). The 3-APTES modified surface, pre-mounted within the microfluidic flow cell was then sequentially exposed to the following solutions:

1)	ethanol (reference)	80 minutes
2)	4-phenylazophenoxyacetyl chloride in DMSO solution	720 minutes
3)	ethanol (reference)	80 minutes

The success of surface functionalisation was interrogated by the change in the Bragg wavelength between the two ethanol reference flows.

It was found that the Bragg wavelength increased by 46 (± 4) pm during attachment of 3-APTES, with a further increase of 761 (± 5) pm on attachment of **4** to the surface. This corresponds to an increase in analyte refractive index (Δn_{anal}) of 5.1 (± 0.4) x 10^{-4} and 8.4 (± 0.1) x 10^{-3} respectively. In contrast, where the procedure to attach **4** onto the sensor was repeated in the absence of a 3-APTES monolayer, no increase in Bragg wavelength was observed. Similarly flowing only solvents over the surface did not give rise to a permanent Bragg wavelength shift.

To confirm the efficacy of this method to fabricate an azobenzene monolayer,[6] the process was replicated on a silica substrate (glass slide) and the absorption spectrum collected, as shown in Figure S6. Photoisomerisation from the *trans*- to the *cis*-isomer was observed upon exposure to UV light at 365 nm (UVP UVGL-25 dual wavelength UV-lamp). Extrapolation from the peak absorption of both the solution phase and tethered phase resulted in an estimate of the surface coverage of 3-5 x 10^{14} azobenzene molecules/cm^{2}. It has been reported that the surface density of hydroxyls on silica is circa. 5 x 10^{14} molecules/cm^2; with the typical maximum surface functionalisation for tethered hydrocarbons of 2-3 x 10^{14} molecules/cm^2.[7] Allowing for the uncertainty in this extrapolation, the absorbance of the azobenzene film indicates a dense monolayer on the surface.

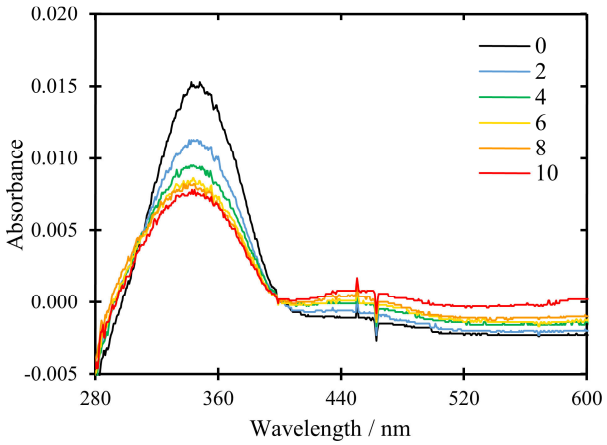

Figure S6. The absorption spectra of **4**, tethered to a silica surface *via* a self-assembled monolayer of 3-APTES, on a silica substrate (black line). Upon exposure to UV light (365 nm) the strong absorption at 348 nm is observed to weaken, corresponding to photoisomerisation from the *trans*- to the *cis*-isomer on the surface; after 10 minutes no further change was observed, indicating a photostationary state was reached. The 'spikes' at 460nm wavelength are an artefact of the spectrophotometer.

S6: INTERACTIONS WITH THE SELF-ASSEMBLED MONOLAYER

Control study in the absence of α-cyclodextrin

Having previously reported that the azobenzene motif exhibits an inherent change in refractive index upon photoisomerisation,[8] a control experiment was performed in the absence of α-CD. It was found that when limited to a single monolayer upon the Bragg grating surface the effects of photoisomerisation of the azobenzene moiety were not detected when immersed in deionised water only, as shown in Figure S7.

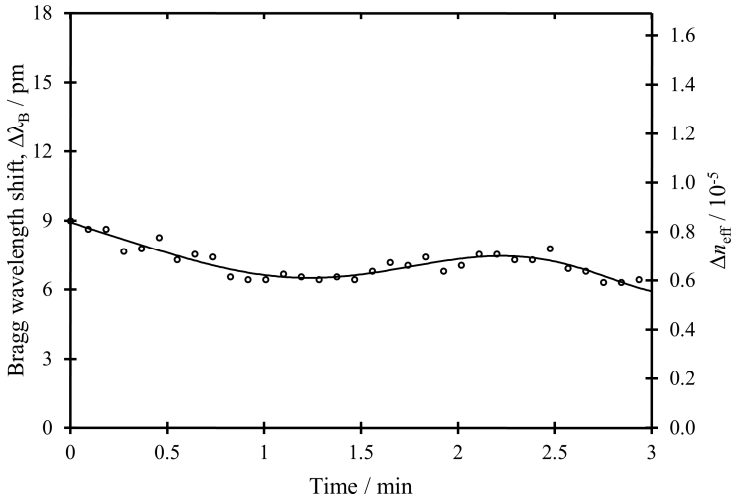

Figure S7. No significant Bragg grating wavelength shift was measured upon exposure to UV light at 365 nm wavelength for 3 minutes, with the variation attributed to minute thermal fluctuations. The *y*-axis is scaled for direct comparison with Figure 3 in the manuscript and the solid line included as a guide for the eye only.

Normalising the Bragg wavelength shift upon binding at the surface for solute refractive index

Figure 4a in the manuscript describes the increase in the average Bragg wavelength differential between the α-CD/*trans*-azobenzene complex and *cis*-azobenzene surfaces, upon increasing the concentration of α-cyclodextrin in the surrounding media. If the recorded shift was solely due to the refractive index change at the surface, it would be expected that there would be a maximum change observed when saturation of surface binding sites was reached. However, this is not evident from Figure 4a, where the Bragg wavelength differential continues to rise with

increasing α-cyclodextrin concentration. This effect is attributed to the d*n*/dc of the α-cyclodextrin solution, in combination with the non-linear sensitivity over large changes in analyte refractive index (dλ/dn_{anal}) that is inherent to evanescent-field sensors, as shown in Figure 2c in the manuscript. The combination of these two factors is that the sensitivity to changes in surface-localised refractive index increase with rising α-cyclodextrin concentration, despite only measuring the differential between the unbound (*cis*-azobenzene) and bound (*trans*-azobenzene) surface within a static reservoir.

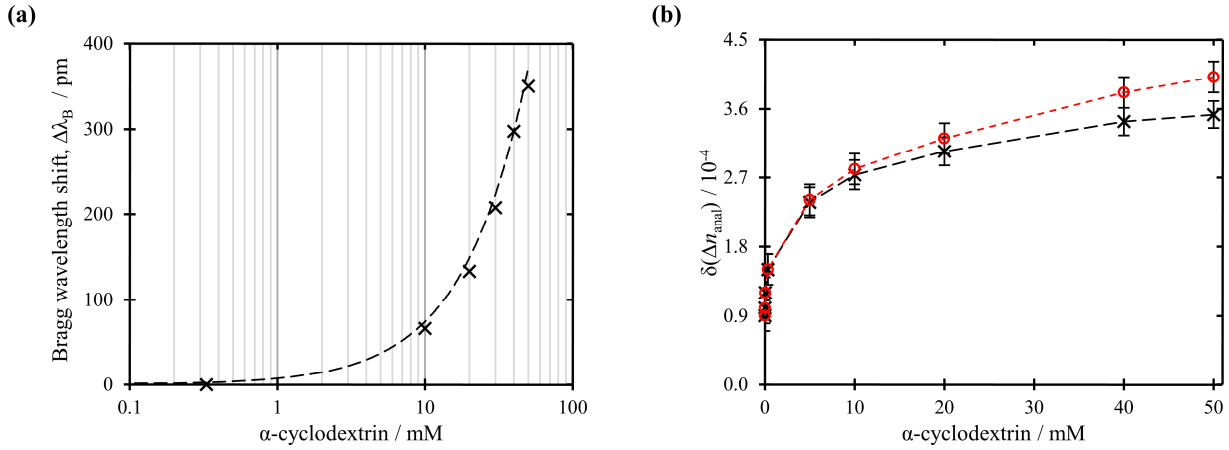

Figure S8. (a) The average Bragg wavelength shift of the 'sensor' gratings as a function of increasing α-CD concentration (points) relative to a baseline of deionised water. This was found to be consistent with the modelled curve, calculated from the reported value of d*n*/dc for an aqueous solution of α-CD of 0.148 cm^3/g (dashed line).[9] **(b)** The difference in analyte refractive index between the α-CD/*trans*-azobenzene complex and *cis*-azobenzene surfaces, δ(Δn_{anal}), upon increasing the concentration of α-CD. For comparison, this was calculated using both the sensitivity of the device in deionised water (red circles), and after correction for the changing sensitivity arising from d*n*/dc of the α-CD solute (black crosses). The dashed lines are a guide for the eye only.

As shown in Figure S8a, increasing the concentration of the solute, α-CD, above 1mM results in a marked increase in the refractive index of the aqueous solution as measured by the 'sensor' Bragg gratings. This increase corresponds to a d*n*/d[α-CD] of 0.141 cm^3/g at 1540-1570 nm wavelengths; this is comparable (allowing for dispersion) with the reported value of d*n*/d[α-CD] of 0.148 cm^3/g measured in water at 675 nm wavelength.[9] The modelled curve was calculated relative to deionised water (*n* = 1.33 RIU) using the reported d*n*/dc, as represented by the dashed line in Figure S8a.

Having determined n_{anal} for each solution, the sensitivity (dλ/dn_{anal}) was then calculated at each concentration from the differential of a polynomial trendline applied to the calibration dataset, shown in black in Figure 2c of the manuscript. It was found that the large increase in concentration from 330 nM to 50 mM resulted in an increase in dλ/dn_{anal} from 49.8 to 56.7 nm/RIU for this device. For reference the sensitivity in ethanol, as used as a reference solvent during monolayer deposition, is calculated as 90 nm/RIU.

The measured Bragg wavelength differential, δ($\Delta\lambda_B$), was converted using the calculated sensitivity at each measured concentration to give the differential in analyte refractive index between the α-CD/*trans*-azobenzene complex and *cis*-azobenzene surfaces, δ(Δn_{anal}), as plotted in Figure S8b (black crosses). For comparison, δ(Δn_{anal}) was also calculated without accounting for the effect of d*n*/dc of the solute (red circles), with the sensitivity of the device in deionised water applied uniformly across the dataset. The correction for solute dn/dc has the effect of flattening the curve at higher concentrations, with the rate of increase of δ(Δn_{anal}) tending towards zero – the gradient is estimated to be 9 x10^{-7} mM^{-1} between 40 to 50 mM, less than the uncertainty in the refractive index measurement. As such, it is expected that any further raise in concentration would not give rise to a measurable increase, indicating saturation of surface binding sites.

It should be noted that within a flow cell the effect of d*n*/dc can be avoided by switching to pure solvent or buffer (as exemplified here during monolayer deposition), as is typically the case in e.g. commercial SPR biosensors. However in the context of supramolecular surfaces, this requires a sufficiently slow dissociation constant for

disassembly to be trackable and is impractical when monitoring a system in dynamic equilibrium. Alternatively, the use of a more tailored solute concentration (i.e. a smaller concentration range or avoidance of higher wt% loadings) would minimise the effect of d*n*/dc.

The rate of association and dissociation as a function of α-cyclodextrin concentration

The time for the Bragg wavelength to shift by half the total differential between the two equilibrium states (c.f. complex 'half-life' time and defined here as 'half-time', $t_{1/2}$) was calculated for the range of different concentrations of α-cyclodextrin. Dissociation of the surface-bound complex appears to be dominated by photoisomerisation of the *trans*-azobenzene guest to the less favoured *cis*-isomer, evidenced by the average dissociation half-time measured to be independent of the α-CD concentration under the illumination conditions of the experiment, as shown in Figure S8. Similarly, the association rate was found to be concentration independent at higher concentrations of α-cyclodextrin, indicating that photoisomerisation is slower than the rate of complex formation. However, with a 330 nM α-CD solution the half-time for assembly doubled (circled in Figure S8), suggesting that at this concentration and below, the kinetics of host-guest complex formation may dominate.

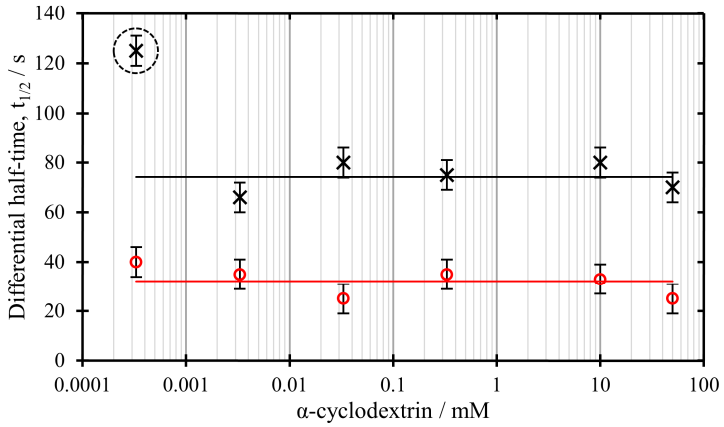

Figure S9. Plot of the complex half-life time for both association (black cross) and dissociation (red circle) as a function of α-cyclodextrin concentration. Lines represent the average duration across all concentrations, with the exception of the circled outlier at 330 nM.

REFERENCES

1. M. Svalgaard and M. Kristensen, *Electron. Lett.*, 1997, **33**, 861–863.
2. G. D. Emmerson, S. P. Watts, C. B. E. Gawith, V. Albanis, M. Ibsen, R. B. Williams, and P. G. R. Smith, *Electron. Lett.*, 2002, **38**, 1531–1532.
3. C. B. E. Gawith, G. D. Emmerson, S. G. McMeekin, J. R. Bonar, R. I. Laming, R. B. Williams, and P. G. R. Smith, *Electron. Lett.*, 2003, **39**, 1050–1051.
4. R. M. Parker, J. C. Gates, M. C. Grossel, and P. G. R. Smith, *Sensors Actuators, B*, 2010, **145**, 428–432.
5. R. M. Parker, J. C. Gates, D. J. Wales, P. G. R. Smith, and M. C. Grossel, *Lab Chip*, 2013, **13**, 377–385.
6. M. Han, T. Honda, D. Ishikawa, E. Ito, M. Harab, and Yasuo Norikane, *J. Mater. Chem.*, 2011, **21**, 4692–4702.
7. R. De Palma, W. Laureyn, F. Frederix, K. Bonroy, J.-J. Pireaux, G. Borghs, and G. Maes, *Langmuir*, 2007, **23**, 443–451.
8. R. M. Parker, J. C. Gates, H. L. Rogers, P. G. R. Smith, and M. C. Grossel, *J. Mater. Chem.*, 2010, **20**, 9118–9125.
9. G. M. Pavlov, E. V. Korneeva, N. A. Smolina, and U. S. Schubert, *Eur. Biophys. J.*, 2010, **39**, 371–379.